MATERIALS SCIENCE

Low-energy room-temperature optical switching in mixed-dimensionality nanoscale perovskite heterojunctions

Ji Hao[1], Young-Hoon Kim[1], Severin N. Habisreutinger[1], Steven P. Harvey[1], Elisa M. Miller[1], Sean M. Foradori[2], Michael S. Arnold[2], Zhaoning Song[3], Yanfa Yan[3], Joseph M. Luther[1]*, Jeffrey L. Blackburn[1]*

Long-lived photon-stimulated conductance changes in solid-state materials can enable optical memory and brain-inspired neuromorphic information processing. It remains challenging to realize optical switching with low-energy consumption, and new mechanisms and design principles giving rise to persistent photoconductivity (PPC) can help overcome an important technological hurdle. Here, we demonstrate versatile heterojunctions between metal-halide perovskite nanocrystals and semiconducting single-walled carbon nanotubes that enable room-temperature, long-lived (thousands of seconds), writable, and erasable PPC. Optical switching and basic neuromorphic functions can be stimulated at low operating voltages with femto- to pico-joule energies per spiking event, and detailed analysis demonstrates that PPC in this nanoscale interface arises from field-assisted control of ion migration within the nanocrystal array. Contactless optical measurements also suggest these systems as potential candidates for photonic synapses that are stimulated and read in the optical domain. The tunability of PPC shown here holds promise for neuromorphic computing and other technologies that use optical memory.

INTRODUCTION

Solid-state optoelectronic memory technologies and optical switches could replace electrically stimulated resistive switches in photonic integrated circuits and dynamically configurable neural networks for energy-efficient brain-inspired (neuromorphic) computing and information processing (*1*–*4*). Artificial optical synapses rely upon the modulation of a material's conductance [or light transmission in the case of photonic synapses (*2*, *3*, *5*)] by light pulses, while learning and memory retention behaviors that mimic the brain generally require gradually tunable conductance amplitude (synaptic weight) and decay dynamics with respect to the properties of input stimuli (e.g., pulse width, intensity, and timing). To achieve these tasks in an energy-efficient manner, optical synapses require switching with low-energy pulses (ideally approaching the brain's scale of ~1 to 100 fJ per spiking event), room-temperature operation at low operating voltages, and facile strategies for analog modulation of synaptic weight. At the material level, optical switching is typically engendered by the realization of persistent photoconductivity (PPC), which can arise from a variety of mechanisms such as ion migration, defect-mediated carrier trapping, optically stimulated phase changes, or energetic barriers that inhibit charge carrier recombination (*6*–*10*).

Metal-halide–based perovskites are semiconductors that can be processed from solution and have enabled a number of high-performance optoelectronic devices (*11*). The soft nature and highly ionic character of the crystal lattice, however, allows migration and diffusion of ionic species at low activation energies (*12*–*15*). Although this ionic motion can have negative effects on device performance of solar cells and light-emitting diodes (LEDs) (*16*, *17*), it also may be harnessed to produce unique devices that exploit the complex interplay between light, voltage, charge carriers, and ions (*15*).

Voltage-induced ion flow is a central process defining the activity of chemical synapses in the nervous system, and many neuromorphic materials and applications use ion-stimulated processes to modulate conductance (*18*). Facile ion migration within perovskites has stimulated interest in electrically stimulated artificial synapses (*19*–*21*). Because illumination can lower ionic migration barriers even further (*22*–*25*), this makes metal-halide perovskites particularly attractive for optical synapses. In this study, we demonstrate that light-induced ion migration in perovskite nanocrystal (NC)–based heterojunctions enables optically stimulated memory and neuromorphic functionality at energy consumption values well below other recently demonstrated optical synapses.

Heterojunctions between dissimilar photo-active nanoscale materials (*10*, *26*), including those based on perovskites (*27*–*30*), have been used in recent studies for realizing PPC and, in some cases, synaptic behavior. PPC in many cases, however, requires cryogenic temperatures (*10*) and/or high operating voltages (*26*, *28*, *30*, *31*), which makes it challenging to achieve low spiking energies. Here, we exploit arrays of inorganic perovskite NCs as the primary absorber layer, based on the recent demonstrations that ion migration is enhanced along grain boundaries and surfaces (*22*) and is prevalent in perovskite NC arrays (*32*, *33*). Highly enriched semiconducting single-walled carbon nanotube (s-SWCNT) networks serve as the charge-separating heterojunction and conducting channel material for NC/SWCNT phototransistors (*34*), based on well-documented exceptional field-effect transistor (FET) performance (*35*–*37*) and efficient charge carrier extraction from perovskite absorber layers (*38*–*40*). The FET geometry enables efficient lateral transport of carriers in the SWCNT channel while simultaneously generating an out-of-plane electric field that can drive ion migration in the NC array to realize PPC. The combination of these strategies allows us to demonstrate room-temperature writing and erasing of optical

---

[1]National Renewable Energy Laboratory, Golden, CO 80401, USA. [2]University of Wisconsin, Madison, WI 53706, USA. [3]University of Toledo, Toledo, OH 43606, USA.
*Corresponding author. Email: jeffrey.blackburn@nrel.gov (J.L.B.); joey.luther@nrel.gov (J.M.L.)

memory, while complementary optical and ion-sensitive mass spectrometry measurements identify ion migration as an important source of PPC. We achieve optical switching at what we believe are the lowest reported pulse energies for optically stimulated electrically read synapses (*1*, *6*, *10*, *27*, *30*, *31*, *41*–*44*) (ca. 7 to 75 fJ per pulse for light solely illuminating the device active area) at no applied gate voltage. PPC stimulated by short light pulses (microseconds to seconds) is retained for thousands of seconds at room temperature and no applied gate voltage, enabling the demonstration of both synaptic plasticity and long-term potentiation. The nearly limitless tunability of these model devices, based on the rich pallet of inorganic and organic constituents as well as the control over NC size and surface chemistry, is promising for the development of a new class of hybrid optical memory devices.

RESULTS AND DISCUSSION

Charge-separating NC/SWCNT bilayer heterojunctions are prepared from thin (ca. 10 nm) electronically coupled s-SWCNT networks, which are coated with 30 to 50 nm of perovskite NCs (edge lengths of 10 to 15 nm; fig. S1). We focus on formamidinium lead bromide ($FAPbBr_3$)–based heterojunctions in the main article and discuss cesium lead iodide ($CsPbI_3$)– and cesium lead bromide ($CsPbBr_3$)–based heterojunctions where appropriate (and in the Supplementary Materials) to show that the strategies demonstrated here apply to other perovskite NC systems. Figure 1A shows absorption spectra for a (6,5) SWCNT network, $FAPbBr_3$ NC array, and $FAPbBr_3$ NC/SWCNT heterojunction. The heterojunction spectrum has a new peak at 1168 nm (labeled X^+), assigned to the creation of charged excitons (trions) in the (6,5) SWCNTs (*45*, *46*), which demonstrates ground-state charge transfer in the heterojunction (see also fig. S3). FET (Fig. 1B and figs. S4 and S5) and Raman measurements (fig. S6) confirm that this ground-state charge transfer is a net transfer of holes from the perovskite NCs to produce p-type SWCNT FET channels. Specifically, the threshold voltages of dark heterojunctions (Fig. 1B, left) are shifted to higher positive voltages than undoped SWCNT FETs, in similar fashion to intentionally p-type doped SWCNT FETs (Fig. 1B, right).

Illumination of heterojunction FETs generates photocurrent [$I_{ph} = I_{light} - I_{dark}$, where I_{light} and I_{dark} are the source-drain currents (I_{DS}) under illumination and in the dark, respectively] and shifts the threshold voltage to a higher positive voltage (Fig. 1B, left). We observe these large photocurrents exclusively for NC/SWCNT heterojunctions and not for neat NC arrays, neat s-SWCNT networks, or heterojunctions prepared with large-diameter, small-bandgap s-SWCNTs (fig. S7). In addition, Fig. 1C and fig. S8 show strong quenching of NC photoluminescence (PL) and reduction in PL lifetime in the heterojunction. These effects result from the type II band offset between the SWCNTs and NCs (Fig. 1D) and demonstrate that photogenerated holes are injected into (6,5) s-SWCNT

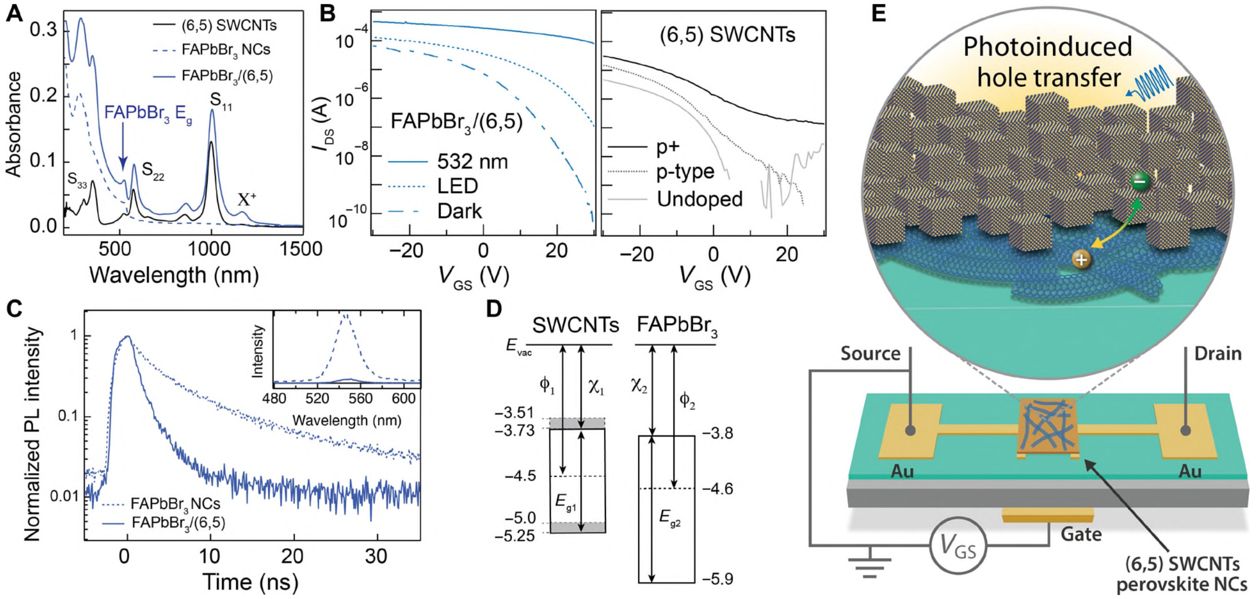

Fig. 1. Ground- and excited-state charge transfer in bilayer NC/SWCNT heterojunctions. (**A**) Absorption spectra of a neat (6,5) s-SWCNT film, $FAPbBr_3$ NC array, and a $FAPbBr_3$ NC/SWCNT heterojunction. SWCNT optical transitions labeled as S_{xx} for excitonic transitions and X^+ for positively charged trion absorption. Absorption spectra of other NC/SWCNT heterojunctions shown in fig. S2. (**B**) FET transfer curves for $FAPbBr_3$ NC/SWCNT heterojunctions (left) in the dark or illuminated with a white LED or 532-nm laser ($V_{DS} = 3$ V). FET curves for other NC/SWCNT heterojunctions shown in fig. S4. FET transfer curves for neat (6,5) s-SWCNT thin films (right) that are undoped (light gray line), lightly p-doped with a one-electron oxidant (triethyloxonium hexachloroantimonate or OA, darker gray line), or heavily doped with OA (black line, p+). All SWCNT transfer curves measured in the dark, $V_{DS} = 3$ V. (**C**) Time-resolved PL (TRPL) decay of the $FAPbBr_3$ 545-nm emission for a neat $FAPbBr_3$ NC array (dashed line) and a $FAPbBr_3$ NC/(6,5) s-SWCNT heterojunction (solid line). Inset shows PL spectra for the same two samples. Excitation at 405 nm. PL and TRPL for other NC/SWCNT heterojunctions shown in fig. S8. (**D**) Energetics estimated for (6,5) s-SWCNT thin film and $FAPbBr_3$ NC array, showing work functions (ϕ_i), electron affinities (χ_i), and electronic band gaps (E_{gi}) of the separate films (before contact). The ultraviolet photoelectron spectroscopy (UPS) data and analysis are shown in fig. S9 for $FAPbBr_3$ NCs. Values for SWCNTs taken from our recent UPS measurements (*39*) and separate calculations (*62*) (upper and lower bounds on gray boxes, respectively). (**E**) Schematic of the FET setup used. The blow-up highlights the NC/s-SWCNT interface and the photoinduced hole transfer event that occurs at this interface to drive the photocurrent observed in phototransistors. Micrographs of typical FET channel shown in fig. S10.

channels from illuminated perovskite NCs (Fig. 1E). It is important to note that DC mobility in the s-SWCNT network (>1 cm^2/Vs) (*47*) is at least four orders of magnitude larger than in the NC array (ca. 10^{-5} cm^2/Vs) (*48*). Thus, lateral hole transport in the s-SWCNT network is the dominant source of dark current and photocurrent in these (photo)transistors.

The NC/SWCNT phototransistors show large photoresponse over several orders of magnitude of incident fluence, as shown in Fig. 2A and fig. S11. Responsivity (R_λ) is calculated as

$$R_\lambda = I_{ph}/(P \times A) \quad (1)$$

where P is the incident light power density and A is the channel area. Responsivity is tunable via V_{GS}, V_{DS}, and excitation wavelength (Fig. 2A).

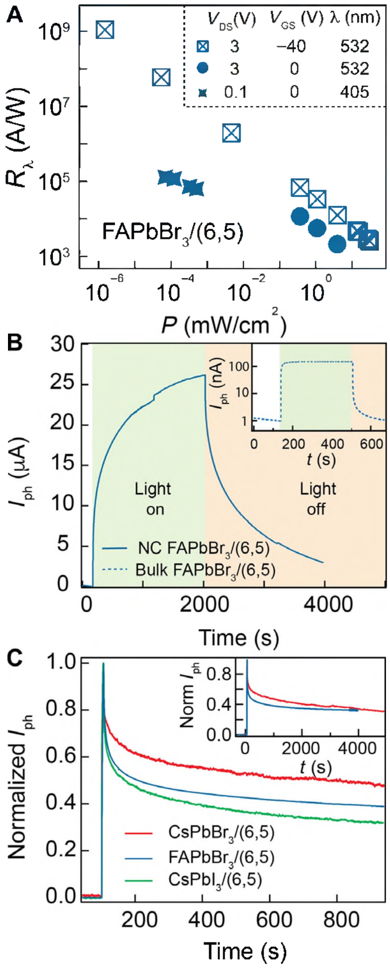

Fig. 2. High responsivity and transient photoresponse in NC/SWCNT heterojunctions. (**A**) Photoresponsivity (R_λ) as a function of incident fluence (continuous excitation) with either 405- or 532-nm laser. Excitation wavelength and bias conditions listed in legend. (**B**) Photocurrent (I_{ph}) as a function of time, V_{GS}, and photoexcitation with a 405-nm laser. Green region highlights the photocurrent rise time during continuous illumination, and orange region highlights the photocurrent decay time after the illumination is turned off. V_{GS} = 0 V and V_{DS} = 0.1 V. Inset shows the same experiment performed on a bulk $FAPbBr_3$/(6,5) sample. V_{GS} = 0 V and V_{DS} = 3 V. (**C**) Stimulation of PPC in the three NC/SWCNT bilayers with 5-s, 405-nm light pulse. Inset shows that the $CsPbBr_3$ and $FAPbBr_3$ heterojunction photocurrent transients last well beyond an hour.

The $FAPbBr_3$ heterojunction responsivity reaches 1.1 × 10^9 A/W at low fluence, in line with some of the highest values achieved for heterojunction phototransistors using high-mobility channels such as graphene and monolayer MoS_2 (*10*, *49*, *50*). The high responsivity and external quantum efficiency values of our perovskite NC/SWCNT heterojunctions can be explained by the quantum gain mechanism (*51*), as discussed in detail in the Supplementary Materials (section S1 and figs. S11 and S12).

While the performance metrics of the heterojunction phototransistors reflect a high efficiency of photoinduced hole transfer (Fig. 1E), Fig. 2B demonstrates that slow transient processes also contribute to the photocurrent rise and decay. Figure 2B shows time-dependent photocurrent of the $FAPbBr_3$ heterojunction phototransistor continuously illuminated with a 405-nm laser (18 mW/cm^2). While a fraction of I_{ph} arises promptly, I_{ph} generally grows in slowly over the course of 30 min. When laser irradiation is turned off, I_{ph} shows an initial decrease followed by a very slow recovery to the dark current, with full recovery not reached even after 30 min. Comparison of these slow kinetics to the fast kinetics observed for a heterojunction between (6,5) SWCNTs and bulk $FAPbBr_3$ thin film (Fig. 2B, inset) indicates that the NC components (likely undercoordinated surfaces and/or mobile NC surface ions, vide infra) are vital to realizing PPC in these heterojunctions. Figure 2C demonstrates that PPC is a universal characteristic of all three NC/SWCNT heterojunctions, in this case stimulated by short light pulses (5 s) and lasting well over an hour (Fig. 2C, inset). Because typical recombination times of charges separated across type II heterojunctions range from picoseconds to microseconds (*45*, *46*), this PPC represents a slowing of the recombination time by anywhere from 9 to >15 orders of magnitude. The short time scales needed to realize PPC are consistent with halide vacancy migration (*15*), as explored in more detail below.

The PPC observed in Fig. 2 does not require application of a gate voltage, contrasting strongly with commonly reported PPC phenomena that arise from substrate-induced charge trapping (*26*, *30*, *41*). In these systems, photocurrent at V_{GS} = 0 V is typically short-lived, whereas application of an appropriate gate voltage leads to longer-lived photocurrent due to charge carrier trapping at the substrate-channel interface. This extrinsic device-related effect is relatively agnostic to the channel material identity and increases the energy consumption for neuromorphic operations due to the need for maintaining large resting voltages. The long photocurrent lifetimes observed here at V_{GS} = 0 V imply that PPC is intrinsic to the NC/SWCNT heterojunction.

To confirm the intrinsic nature of PPC and identify its source, we performed a series of complementary measurements. First, we tracked the time-dependent static absorption spectrum of the s-SWCNT layer within continuously illuminated heterojunctions (Fig. 3A and figs. S13 to S15). Under illumination, the (6,5) S_{11} peak slowly bleached and the trion peak X^+ continuously grew. S_{11} and X^+ then slowly recovered when the laser is turned off. Because the S_{11} bleach and X^+-induced absorption both correlate to the charge carrier density in the s-SWCNTs (*45*), this experiment confirms that the SWCNT hole density increases during continuous illumination under open-circuit conditions and these holes then slowly recombine with electrons when illumination is halted.

Second, because recent studies demonstrate that chemical reactions can occur between noble metal electrodes and lead halide perovskites (*52*, *53*), one could envision that the magnitude of charge

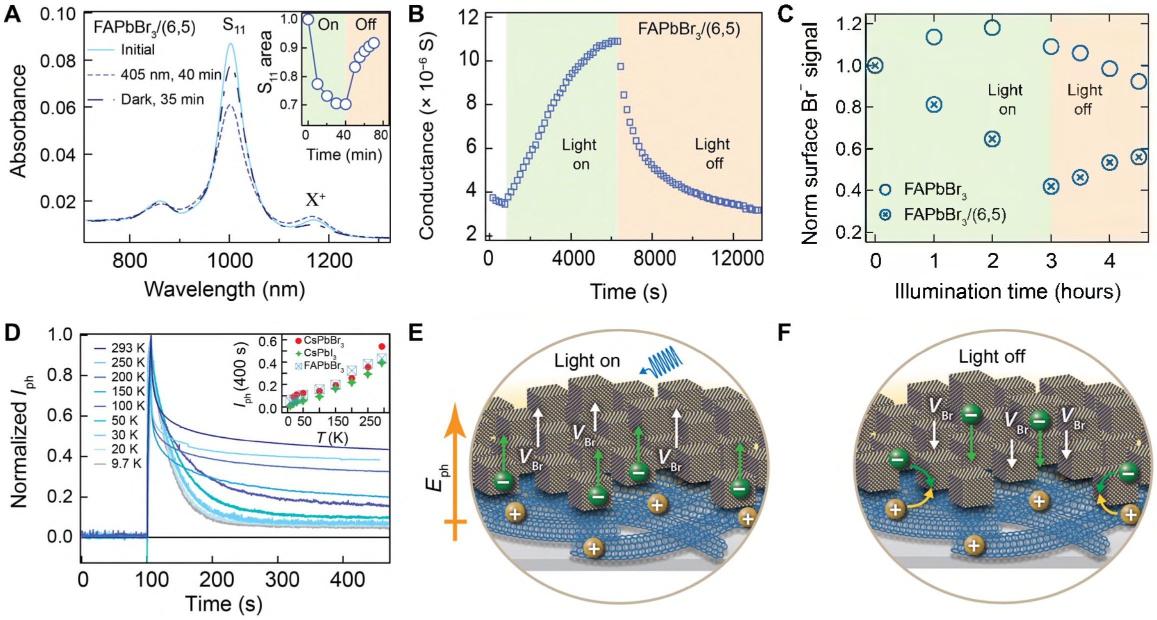

Fig. 3. Tracking PPC and ion migration in NC/SWCNT heterojunctions. (**A**) Time-dependent static absorption spectra in the near-infrared region (highlighting changes to S_{11} and X^+ peaks) for unilluminated $FAPbBr_3$ NC/SWCNT heterojunction, after 40 min of continuous 405-nm illumination, and after the 405-nm illumination is ceased (after 40-min illumination) for 35 min. Inset shows the temporal changes to the s-SWCNT S_{11} area during the continuous illumination phase (green region) and after the illumination is turned off (orange region). (**B**) Slow growth of 9-GHz conductance during continuous illumination (green region) and slow decay (orange region) after 532-nm laser is turned off. (**C**) Normalized surface bromine concentration, as measured by TOF-SIMS, for a $FAPbBr_3$ NC array and a $FAPbBr_3$/(6,5) heterojunction, as a function of continuous illumination time with a 405-nm laser. (**D**) Temperature-dependent photocurrent decay transients of $FAPbBr_3$/(6,5) heterojunction, photoexcited at 405 nm for 5 s with a fluence of 18 mW/cm^2. $V_{GS} = 0$ V and $V_{DS} = 0.1$ V. Inset shows the dependence of the photocurrent at 400 s [I_{ph} (400 s)] as a function of temperature. (**E** and **F**) Schematics of field-induced bromine vacancy (V_{Br}) ion migration during illumination (E) and slower ion diffusion when light is turned off (F).

injection barriers at the source/drain gold electrodes changes during illumination. To rule out any electrode effects, we measured conductance of the $FAPbBr_3$ NC/SWCNT heterojunction with 9-GHz contactless microwave conductivity (Fig. 3B and fig. S16) (*47*). During illumination, the sample conductance slowly increases over the course of ca. 1.5 hours and then decays over another 1.5 hours when the laser is turned off. Because this contactless measurement uses no electrodes, this result demonstrates that the slow transient photoresponse is intrinsic to the NC/SWCNT heterojunction. Beyond confirming the intrinsic nature of the PPC response, the strong and continuously tunable optical responses in the near-infrared and gigahertz regimes (Fig. 3, A and B) suggest these NC/SWCNT heterojunctions as candidates for photonic synapses where synaptic functions are modulated and read entirely in the optical domain (*2*, *3*).

Because the time scales of the slow growth and decay of I_{ph} and optical responses are consistent with recent reports of ion migration–induced poling in lead halide perovskites (*15*), we hypothesized that the slow I_{ph} transients in heterojunctions may arise from a dynamic ionic contribution. To elucidate the role of ion migration and explain the observed PPC in NC/SWCNT heterojunctions, we chemically probe ion movement using time-of-flight secondary ion mass spectrometry (TOF-SIMS) (*54*, *55*). In this experiment (Fig. 3C), the time-dependent surface concentration of bromine in a $FAPbBr_3$ NC/SWCNT heterojunction was measured after different illumination times with a 405-nm laser. The bromide surface concentration in the heterojunction gradually decreased during 405-nm laser illumination and slowly recovered after halting illumination. In contrast, the bromide surface concentration does not decrease in an illuminated $FAPbBr_3$ NC array not in contact with (6,5) s-SWCNTs. These results provide strong evidence that the slow transient photoresponse is coupled to a similar transient response in ion distribution within the perovskite NC array.

Because ion migration should be thermally activated, we performed temperature-dependent photocurrent measurements for heterojunction samples photoexcited with 5-s light pulses (Fig. 3D and fig. S17). I_{ph} decays rapidly at temperatures less than 20 K, whereas transients taken at $T \geq 20$ K all feature substantial PPC that lasts beyond 500 s. The inset of Fig. 3D demonstrates that the residual photocurrent at 400 s [I_{ph} (400 s)] increases systematically with increasing T for all NC/SWCNT heterojunctions. In addition, photocurrent activation energies above 20 K (fig. S17) for the three heterojunctions fall in the range of ca. 3 to 6 kJ/mol (0.027 to 0.06 eV). These values are on the low end reported for halide vacancy migration in illuminated lead-halide perovskites (*12*, *13*, *22*, *24*), consistent with recent studies demonstrating that this activation energy decreases markedly with decreasing grain size (*22*).

The observations in Fig. 3 are consistent with a field-induced migration of bromide vacancies away from the s-SWCNT channel during illumination where they accumulate at the surface of the NC array (Fig. 3E), equivalent to the accumulation of bromide anions at the NC/SWCNT interface. The slow temporal rise of I_{ph} may stem from a modulation of the interfacial energetics as ions redistribute, because interfacial dipoles are known to induce large shifts in band energies (*56*). It is also possible that the slow migration–induced halide accumulation at the NC/SWCNT interface during illumination induces a transient "top gate" that contributes to the slow rise of the hole current in the s-SWCNT channel, because halogens are known to dope carbon nanotubes p-type (*57*). The distances traveled by ions should depend on the illumination duration. Short light pulses (Figs. 2C, 3D, and 4) likely correspond to migration within a single NC (e.g., to the surface), while continuous illumination from minutes to hours (Figs. 2B and 3, A to C) may correspond to migration through the thickness of the array. The magnitude of PPC correlates with the number density of ions that undergo thermally activated migration over the duration of a laser pulse at a given temperature (Fig. 3D). The illumination interval establishes a new equilibrium of positively charged halide vacancies, away from the NC/SWCNT interface, that likely trap electrons via Coulomb attraction. When illumination is turned off (Fig. 3F) and the photoinduced field is reduced, the substantially larger activation barrier for ion diffusion, relative to the migration barrier for drift under illumination (*22–24*), is thus responsible for the slow ion redistribution, electron-hole recombination, and photoconductivity decay.

The PPC demonstrated here for perovskite NC/SWCNT heterojunctions is attractive for developing nonvolatile optical memory devices. Neuromorphic devices aim to emulate analog signal processing behaviors of synapses, whereby low-energy electrical pulses (presynaptic inputs or "spikes") induce postsynaptic currents with continuously tunable "weight." Energy consumption is an important metric for neuromorphic devices. PPC in the perovskite NC/SWCNT heterojunctions enables room-temperature optical memory with no applied gate voltage. This behavior contrasts strongly with recent

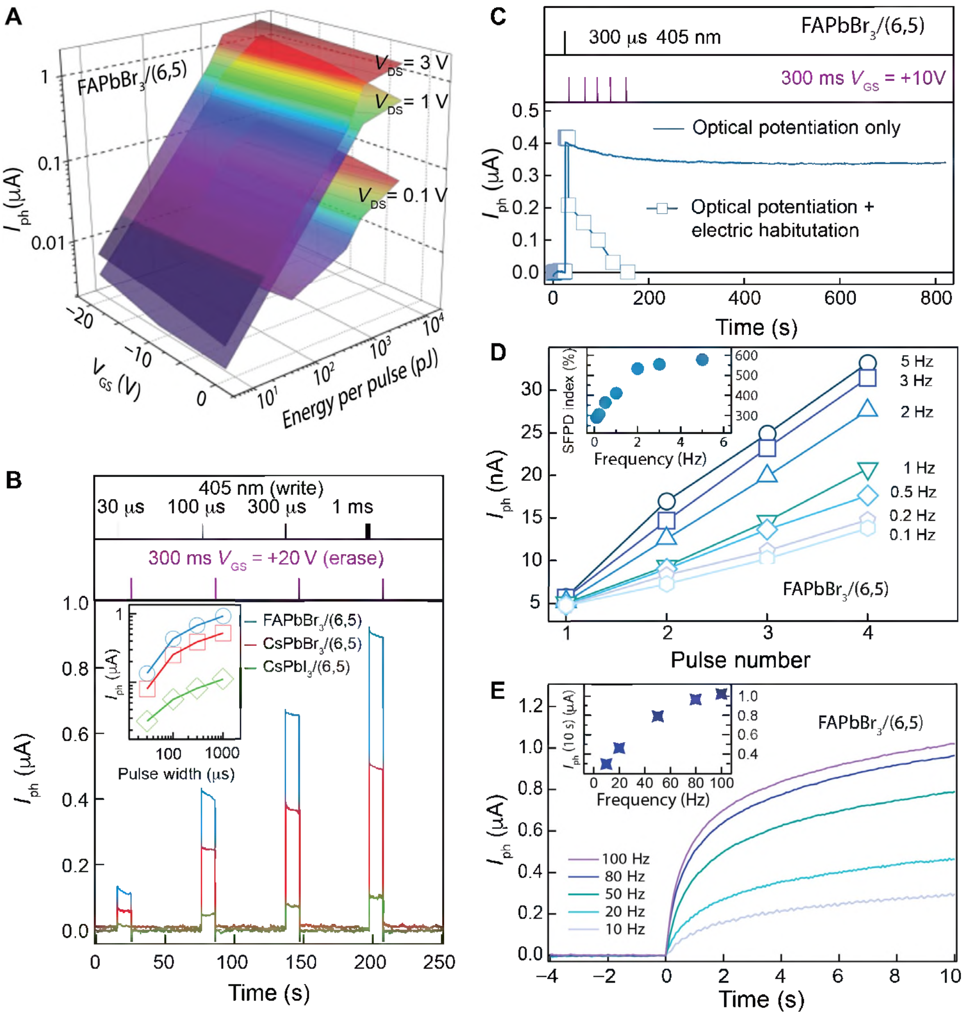

Fig. 4. Basic synapse-like functions with NC/SWCNT phototransistors. (**A**) Dependence of photocurrent for $FAPbBr_3$ NC/SWCNT phototransistor as a function of gate voltage (V_{GS}), source-drain voltage (V_{DS}), and the energy per 30-μs 405-nm pulse. (**B**) Writing and erasing photocurrent in NC/SWCNT phototransistors at low applied bias (steady-state biases of $V_{GS} = 0$ V and $V_{DS} = 0.1$ V). Main plot shows I_{ph} for the three photoexcited NC/SWCNT phototransistors under conditions of identical photon fluence (photons $cm^{-2}\,s^{-1}$) within pulses with varying pulse width. Ten seconds after each light pulse writes a photocurrent, the photocurrent is erased with a 300-ms gate voltage pulse ($V_{GS} = +20$ V). Inset shows I_{ph} as a function of pulse width for the three phototransistors. (**C**) Comparison of $FAPbBr_3$ NC/SWCNT phototransistor that is potentiated with a 300-μs 405-nm pulse and either left to decay naturally (dashed line) or electrically habituated with five consecutive $V_{GS} = +10$ V, 300-ms gate pulses. Steady-state biases of $V_{GS} = 0$ V and $V_{DS} = 0.1$ V. (**D**) Photocurrent in $FAPbBr_3$ NC/SWCNT heterojunction phototransistor as a function of pulse number for four consecutive 30-μs 405-nm pulses delivered at different frequencies. Inset shows the frequency-dependent SFPD index, calculated as the percentage increase in photocurrent measured after the fourth pulse compared to the photocurrent measured after the first pulse. Steady-state biases of $V_{GS} = 0$ V and $V_{DS} = 0.1$ V. (**E**) Photocurrent in $FAPbBr_3$ NC/SWCNT heterojunction phototransistor as a function of time for 30-μs 405-nm pulses delivered at different frequencies. Inset shows the frequency-dependent I_{ph} measured at 10 s after initiation of the pulse train. Steady-state biases of $V_{GS} = 0$ V and $V_{DS} = 0.1$ V.

demonstrations of optical memory requiring low temperatures ($T < 180$ K) (*10*) due to the PPC effect being driven by a small thermodynamic barrier to recombination or requiring large gate voltages to localize carriers (*26*, *30*, *41*, *42*).

Figure 4A demonstrates that NC/SWCNT heterojunction phototransistors can be optically switched with short light pulses at spiking energies that approach the low energies of synapses in the brain. With no applied gate voltage ($V_{GS} = 0$ V and $V_{DS} = 0.1$ V), 30-μs pulses induce persistent 2-nA photocurrents at 84 pJ per spiking event (fig. S19). Because the total energy delivered by the light pulse counts toward energy consumption, this calculation (see section S2) considers the entire power delivered by a light pulse, although our device active area covers only ~0.1% of the total illuminated area. The lowest room-temperature spiking energy we are aware of—37 pJ—was recently reported for perovskite NC/graphene phototransistors (*30*), but that calculation only considers the fraction of incident light striking the 5 μm × 10 μm device area, and the device required high operating voltages ($V_{GS} = 10$ V and $V_{DS} = 0.5$ V). If we calculate our spiking energy in the same manner, the 2-nA spiking event consumes 75 fJ, about 500 times less than this recent report (*30*). This low (and unoptimized) spiking energy compares well to those reported recently for optical synapses, of which most fall in the nJ range per spiking event when normalized to device active area [see table S1 and references therein (*1*, *6*, *10*, *27*, *30*, *31*, *41*–*44*)]. The optical energy input can be further lowered by tuning V_{GS} and V_{DS} (Fig. 4A and figs. S19 to S27) with the caveat that doing so increases the steady-state energy required to maintain the gate and source-drain bias. Increasing only V_{DS} ($V_{GS} = 0$ V and $V_{DS} = 1$ V) enables similar optical switching at 7.4 pJ per spiking event (total energy per pulse), and increasing both V_{GS} and V_{DS} ($V_{GS} = -20$ V and $V_{DS} = 3$ V) allows switching at ca. 740 fJ (total energy per pulse). These spiking energies are substantially lower than other recently demonstrated optical synapses and demonstrate that appropriate light management provides a clear path forward to the fJ energy consumption scale found in the brain.

Synaptic plasticity refers to the tuning of synaptic weight via control over the amplitude (spike intensity), duration (spike pulse width), and temporal dynamics (spike frequency and timing) of spiking events (*21*, *58*). Artificial synapses should ideally have continuously tunable synaptic weight that can be increased or decreased (habituated) via optical or electrical stimuli. Figure 4 (A and B) demonstrates that tunable synaptic weight can be programmed by varying the laser pulse power (at a given pulse width) and width (at a given power). A short gate voltage pulse ($V_{GS} = +20$ V, 300 ms) can completely erase the photocurrent programmed by the laser "write" pulse, as shown in Fig. 4B. In contrast, smaller gate pulse voltages enable gradual photocurrent depression via electric habituation (e.g., $V_{GS} = +10$ V, 300 ms; Fig. 4C).

Spike frequency–dependent plasticity (SFPD) involves the dependence of postsynaptic weight on presynaptic spike frequency, and in the brain, SFPD is believed to underlie learning and associative memory. Figure 4D compares the synaptic weight delivered by four consecutive 30-μs pulses delivered at frequencies ranging from 0.1 to 5 Hz. The SFPD index [Fig. 4D, inset, as defined by Kim *et al.* (*21*)] doubles upon increasing spike frequency from 0.1 to 5 Hz, a result that compares well to previously reported perovskite-based artificial synapses due to the good long-term potentiation realized in our devices (*21*). Figure 4E demonstrates that this plasticity can also be realized in the time domain, with the synaptic weight delivered after 10 s of repetitive 30-μs pulses increasing more than threefold as spiking frequency increases from 10 to 100 Hz.

An important consideration for device fabrication is the scaling down of device dimensions to increase the density of synaptic elements. In addition to increasing density, down-scaling can increase device performance, yielding larger on-currents per unit width of channel (i.e., A μm^{-1}) and transconductance per width of channel (i.e., S μm^{-1}), especially when arrays of aligned s-SWCNTs, as opposed to thin-film s-SWCNT networks, are used (*35*, *36*). Thus, we sought to demonstrate the viability of our mixed-dimensionality perovskite NC/SWCNT optical synapses in short-channel architectures, as demonstrated by proof-of-concept results in Fig. 5. Aligned arrays of (6,5) s-SWCNTs were produced by a floating evaporative self-assembly (FESA) technique, and bottom-gated/top-contacted

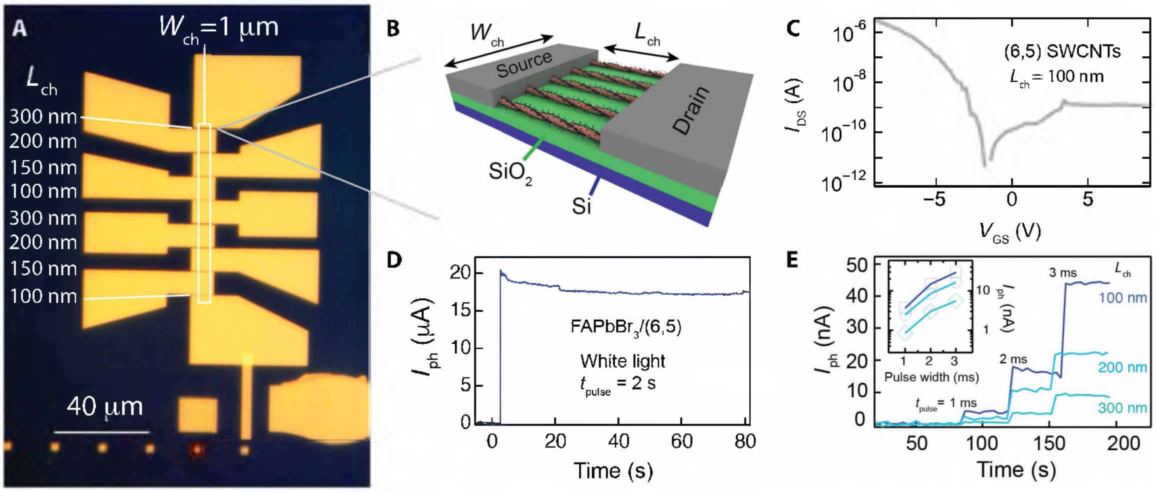

Fig. 5. Short-channel NC/SWCNT optical synapses. (**A**) Optical micrograph of finished short-channel FETs with eight different devices. Channel width of all devices is 1 μm, shown by the white box (not to scale), and channel lengths are listed on the left of the image. (**B**) Cartoon schematic of aligned s-SWCNTs across the source-drain channel. (**C**) Forward scan transfer curve for (6,5) s-SWCNT FET in the dark. (**D**) Photocurrent initiated in a FAPbBr$_3$ NC/SWCNT short-channel ($L_{ch} = 150$ nm) phototransistor by a 2-s white light pulse. $V_{DS} = 0.1$ V and $V_{GS} = 0$ V. (**E**) Photocurrent delivered by short 405-nm laser pulses ($t_{pulse} = 1$, 2, and 3 ms) for short-channel NC/SWCNT optical synapses with $L_{ch} = 100$, 200, and 300 nm. $V_{DS} = 0.1$ V and $V_{GS} = 0$ V. Inset shows the dependence of the induced I_{ph} on the pulse width for each heterojunction.

FETs were fabricated out of these aligned arrays (*35*). Figure 5A displays a microscope image of a finished set of eight devices with channel lengths varying from 100 to 300 nm. Well-isolated individual (6,5) s-SWCNTs span the source-drain channel (Fig. 5B), with scanning electron microscopy (SEM) images showing good alignment and suggesting a packing density of ≥36 nanotubes/μm of channel width (fig. S28). Before NC deposition, the best (6,5) FETs (L_{ch} = 100 nm) produce on/off ratios of five to six orders of magnitude (Fig. 5C), with on-state conductance values in the range of ca. 40 to 60 $\mu S\ \mu m^{-1}$. These conductance values are about an order of magnitude lower than champion values obtained for large-diameter/small-bandgap (≈1.4 nm, $E_g \approx 0.85$ eV) arc discharge s-SWCNT array FETs for the same 100-nm channel length. We attribute these lower conductance values to reduced carrier mobility and increased contact resistance, as expected for small-diameter/large-bandgap ($d \approx 0.76$ nm, $E_g \approx 1.5$ eV) (6,5) s-SWCNTs. While these conductance values can still be optimized, they are nearly 1000× higher than the on-state conductance values realized for thin-film (6,5) FETs (Fig. 1B).

When a thin layer of $FAPbBr_3$ NCs is deposited on top of the aligned (6,5) SWCNTs in the short-channel transistors, the resulting heterojunction phototransistors display optical synapse behavior. Figure 5D demonstrates that a 2-s pulse of white light (beam diameter of ~0.8 mm) induces PPC in the short-channel optical synapse. Figure 5E demonstrates that the synaptic weight can be tuned by the pulse width for short (1 to 3 ms) 405-nm pulses, in similar fashion to the thin-film optical synapses. For this experiment, we use a similar unfocused 405-nm laser (beam diameter = 0.26 cm) for comparison of the switching energy to the thin-film optical synapses. For a channel length of 100 nm, a 1-ms pulse induces 4-nA photocurrent with a total pulse energy of 415 nJ. Normalizing this switching energy to the amount of light absorbed by the active area of the device (100 nm × 1 μm) yields a switching energy of 7.4 fJ per spiking event, an order of magnitude improvement over the thin-film optical synapses discussed in Figs. 1 to 4. I_{ph} varies linearly and inversely with L_{ch} for a given pulse energy, in similar fashion to the dark conductance (floating gate) of as-prepared SWCNT FETs (fig. S29), suggesting that the photocurrent is limited by the SWCNT channel characteristics.

We close by considering some of the practical aspects related to incorporating optical synapses, such as those reported here, into neuromorphic devices. First, one could envision using these optical synapses as elements in visual perception systems. In the simplest embodiments of these types of visual perception systems, spatially arranged arrays of optical synapses can reproduce images that are incident on the array, due to the correlation between the real-space position and photon density of an image incident on the array (*1*, *30*). Neuromorphic functionality is embodied in these systems when they can respond in real time (e.g., to short light pulses) with time-dependent plasticity, both of which are characteristic behaviors of the optical synapses demonstrated here. Further, the performance demonstrated here compares well to recent demonstrations of optical synapses for neuromorphic visual perception systems, because we show neuromorphic functionality at substantially shorter optical pulse widths [nanoseconds to microseconds compared to ≥200 ms (*1*) and ≥5 s (*30*)] and lower switching energies [<75 fJ per pulse, compared to 14 nJ per pulse (*30*) and 37 pJ per pulse (*30*) when normalized to device area]. These metrics bode well for the integration of our optical synapses into visual perception systems that can perform in challenging environments with short light pulses and ultralow light levels.

One can also consider the integration of these elements into neural networks with other resistive switching elements. As an example, in section S3, we consider a scenario in which one or more optical synapses feed into an artificial "soma" that consists of a prototypical state-of-the-art VO_2 resistive switching element (*59*, *60*). In this hypothetical system, a VO_2 neuronal spiking event is predicated on reaching a threshold charge density that triggers a current-induced insulator-to-metal (IMT) transition and sends a current spike as an output signal. If we consider the performance of our devices at the lowest photon fluences and applied potentials (corresponding to 2- to 4-nA currents for 7.4- to 75-fJ short-pulse spiking events at V_{GS} = 0 V and V_{DS} = 0.1 V), only a few tens to hundreds of optical pulses are needed to trigger the VO_2 IMT. This conservative estimate is reduced if we slightly increase the applied potential, photon fluence, or pulse width (Fig. 4A), and the current needed to switch the VO_2 element could also be integrated across a number of optical synapses (tens to hundreds).

We put the performance metrics of our optical synapses into context by comparing to recent literature reports (*1*, *6*, *10*, *27*, *30*, *31*, *41*–*44*) in table S1. The hybrid NC/SWCNT synapses outperform recent demonstrations of optically stimulated and electrically read synapses across a number of important metrics. They produce long-lived photocurrent at low overall energy consumption by responding to low-energy optical pulses at low operating voltages and at room temperature. Another differentiation of this result is the shorter activation pulses of only 30 μs to produce persistent photocurrent, with microwave conductivity results showing optical conductance changes imparted by 5-ns pulses. This contrasts with recent demonstrations that use light pulses in the range of 1 ms to 5 s (table S1). Further, the demonstration of successful optical switching down to channel lengths of 100 nm (smallest device area in table S1) suggests that these high-performance optical synapses can ultimately be integrated at high density into a variety of emerging neuromorphic applications.

In this work, we designed heterostructures between perovskite NCs and highly enriched semiconducting SWCNTs that enable exceptionally long-lived PPC and function as optically stimulated synapses. Detailed analysis demonstrates that PPC is an intrinsic property of these nanoscale heterojunctions, enabled by a transverse field-driven ion migration process that may capitalize upon the undercoordinated surfaces of NCs and the phototransistor geometry. The high responsivity and intrinsic PPC response of these artificial optical synapses enable synaptic stimulation at low optical pulse energies and operating voltages. Initial demonstrations of basic neuromorphic functions suggest that a wide variety of spiking behaviors and synaptic plasticity behaviors may be realized in these heterojunctions through both material modifications and the broad array of available experimental knobs (V_{GS}, V_{DS}, P_{laser}, pulse width, pulse frequency, etc.). Ultimately, our results provide previously lacking design principles for a versatile class of nanoscale heterojunctions that can be incorporated into energy-efficient optical memory and neuromorphic computing applications.

MATERIALS AND METHODS

Chemicals

Formamidinium acetate (FA-acetate; 99%), cesium carbonate (Cs_2CO_3; 99.9%), $PbBr_2$ (≥98%), oleic acid (OA; technical grade 90%), oleylamine (OAm; technical grade 70%), 1-octadecene (1-ODE; technical grade 90%), hexane (reagent grade ≥95%), octane (anhydrous, ≥99%), methyl acetate (MeOAc; anhydrous, 99.5%), sodium borohydride

($NaBH_4$, ≥98%), cesium toluene (anhydrous, 99.8%), and ethanol (EtOH, 200 proof, ≥99.5%) were purchased from Sigma-Aldrich. Lead (II) iodide (PbI2, 99.9985%) was purchased from Alfa Aesar.

Synthesis of $CsPbBr_3$ NCs

In a three-necked round-bottom flask, 1.25 mmol (0.407 g) of Cs_2CO_3, 20 ml of 1-ODE, and 1.25 ml of OA were degassed under vacuum at room temperature and then at 50°C for 30 min. The temperature was then increased to 120°C under N_2 and kept at this temperature for injection. In another three-necked round-bottom flask, 1.08 mmol (0.407 g) of $PbBr_2$ and 25 ml of 1-ODE were degassed under vacuum at room temperature and at 120°C for 30 min. Mixtures of 7.56 mmol (2.5 ml) of OA and 7.56 mmol (2.5 ml) of OAm were preheated to 120°C and then injected into the $PbBr_2$ mixture under vacuum. After $PbBr_2$ was fully dissolved, the temperature of the solution was increased to 180°C. Under N_2 flow, 2 ml of the Cs-oleate stock solution was swiftly injected into the $PbBr_2$ mixture, which was then quenched by immersing the flask in an ice bath.

Synthesis of $FAPbBr_3$ NCs

In a three-necked round-bottom flask, 15 mmol (1.563 g) of FA-acetate, 15 ml of OA, and 15 ml of ODE were degassed under a vacuum at room temperature and then at 50°C for 30 min. The temperature was then increased to 120°C under N_2 and kept at this temperature for injection. In another three-necked round-bottom flask, 0.74 mmol (0.2738 g) of $PbBr_2$ and 25 ml of 1-ODE were degassed under vacuum at room temperature and at 120°C for 30 min. Mixtures of 12.1 mmol (4 ml) of OA and 3.025 mmol (1 ml) of OAm were preheated to 120°C and then injected into the $PbBr_2$ mixture under vacuum. After $PbBr_2$ was fully dissolved, the temperature of the solution was increased to 160°C. Under N_2 flow, 5 ml of the FA-oleate stock solution was swiftly injected into the $PbBr_2$ mixture, which was then quenched by immersing the flask in an ice bath.

Purification of NCs

MeOAc (50 ml) was added to the as-synthesized $CsPbBr_3$ NCs and $FAPbBr_3$ NCs. After the mixed solutions were shaken a few times, they were centrifuged at 7500 rpm for 5 min. The resulting precipitate was dispersed in 5 ml of hexane, and then 10 ml of MeOAc was added again followed by centrifugation at 7500 rpm for 5 min. The precipitate was collected and redispered in 5 ml of octane to coat the film.

Synthesis of $CsPbI_3$ NCs

$CsPbI_3$ NCs were synthesized and concentrated in an octane/hexane solution using previously published methods (*1*). For most of the films in this work, the temperature of the solution containing PbI_2, ODE, OA, and OAm was raised to 185°C at the time of injection of the Cs-oleate solution, with a reaction time of 5 s before quenching in an ice bath.

NC film deposition

The 1 inch × 1 inch glass substrates (Abs, PL) or 1 cm × 2 cm quartz substrates (for microwave conductivity measurements) were sonicated in isopropanol and then acetone for 10 min each, followed by a 10 minute ultraviolet-ozone treatment. The following deposition process was done in a flow box kept at ~20% humidity: The NC solution was spin-cast onto the glass substrate at 1000 rpm for 20 s and then 2000 rpm for 5 s. The film was then dipped three times in quick succession into dry methyl acetate (MeOAc), which was rapidly dried off using an N_2 gun.

Preparation of polymer and s-SWCNT dispersion

SG65i SWCNT material, prepared by the CoMoCAT^{TM} method, was purchased from Chasm. The polymer used in this study was poly[(9,9-dioctylfluorenyl-2, 7-diyl)-alt-co-(6,6′-[2,2′-bipyridine])] (PFO-BPy) purchased from American Dye Source. 10 mg of SWCNT powder and 40 mg of PFO-BPy were placed into 20 mL of toluene. This mixture was sonicated by using a tip sonicator (Cole-Parmer CPX 750) for 30 min. This dispersion was then centrifuged at 13200 rpm for 5 min. (Beckman Optima L-100XP ultracentrifuge, SW32 Ti rotor). The (6,5)-enriched supernatant was extracted by pipette. Then, most of the excess polymer was removed by performing two to three 20-hour ultracentrifuge runs at 24100 rpm. After each 20-hour run, the dark SWCNT pellet was redispersed into toluene by bath sonication.

Fabrication of FET device

The typical device was fabricated on a 200-nm-thick SiO_2/highly doped Si wafer (1 to 10 ohm·cm) purchased from MTI Corporation by using the standard optical lithography technique. 5-nm-thick Ti and 20-nm-thick Au electrodes were deposited on the patterned device in a thermal evaporation deposition system, and the gate electrode was directly contacted with highly doped Si wafer. All the procedures were performed in the cleanroom. The designed channel lengths (L_{ch}) of the typical device are 5, 10, and 25 μm, and the channel width (W_{ch}) is 1000 μm.

Deposition of arrays of aligned s-SWCNTs and fabrication of array FETs

Following the final 20-hour centrifugation run, purified (6,5) s-SWCNTs were dispersed in chloroform to a concentration of 3 mg ml^{-1} and then deposited on 15-nm SiO_2/highly doped Si wafer pieces using the FESA alignment process described previously (*35*) using a substrate lift rate of 5 mm min^{-1} and a s-SWCNT ink flow rate of 175 μl min^{-1}. Devices were fabricated using a three-step electron beam lithography process using poly(methyl methacrylate) (PMMA) 950 as a positive resist. In the first step of fabrication, alignment marks were written and fabricated using 0.7/9.3 nm of thermally evaporated Cr/Au. Cross-polarized optical microscopy was used to locate the position of FESA-aligned s-SWCNT stripes with respect to the alignment marks for further device fabrication. Using those marks, a second lithography process exposed the future electrode areas and defined 1-mm-wide channels of s-SWCNT protected by PMMA. Cross-polarized optical microscopy was used again to confirm that the protected channel regions were on well-aligned stripes of s-SWCNTs. The undesired s-SWCNTs outside the channel region were removed using an oxygen reactive ion etch, leaving the protected channels of aligned s-SWCNTs intact. A third lithographic step defined the electrode pads using 10/20 nm of thermally evaporated Pd/Au followed by a standard liftoff process. Each 1-mm-wide channel of aligned s-SWCNTs contained devices with channel lengths of 100, 150, 200, and 300 nm for a total of eight devices on each defined s-SWCNT stripe.

Preparation of SWCNT/perovskite NC heterojunction film

Semiconducting SWCNT networks were prepared by spraying the prepared s-SWCNT inks onto the prepared substrate (SiO_2/Si wafer or quartz substrate) using an ultrasonic sprayer with a Sonotek 120-kHz impact nozzle. The s-SWCNT solution was sprayed at 300 μl/min, controlled by using a syringe pump under the 7 standard liter/min nitrogen flow with a 0.8-W spray nozzle power at room temperature. The substrate was normally heated up to about 130°C when spraying. After the spray coating, the s-SWCNT thin film was soaked in a 78°C toluene solution for 10 min to remove the excess fluorene-based polymers. After depositing the SWCNT networks, the perovskite thin films were then prepared by spin coating the NC solution onto the prefabricated device by using a spin rate of 3000 rpm for 30 s, followed by annealing at 150°C for 30 min on the hotplate in the nitrogen-filled glove box.

Scanning electron microscopy

The morphologies and microstructures of the prepared perovskite NCs with (6,5) SWCNTs were investigated using a field-emission SEM (Hitachi S-4800); samples were imaged at 3-kV acceleration and 7- to 10-mm working distance.

Ultraviolet-visible near-infrared absorbance measurement

Absorbance measurements were performed on an Agilent Cary 5000 spectrophotometer and an Agilent Cary 7000 spectrophotometer, with a step size of 2 nm and a scanning speed of 600 nm min^{-1}. The blank substrate was calibrated as the baseline before the film measurement.

High-resolution confocal Raman spectra microscope characterization

Raman characterization of was performed by using the high-resolution confocal Renishaw inVia Raman Microscope (RE04) System with Wire 5.0 control software. The applied laser excitation wavelength is 785 nm (1.58 eV), the exposure time was 1 s per spectrum, with 600 lines per millimeter grating, and the laser intensity ratio was set to 0.01% with 100× objective lens.

FET measurement

The typical FET measurement was set up and performed in the N_2-filled glove box, which consists of two Keithley 2400 source meters, controlled by LabVIEW. One Keithley 2400 source meter was used to supply the source-drain voltage (V_{DS}) and monitor the channel current (I_{DS}), and the other source meter was used to supply the gate voltage (V_{GS}) and monitor the gate leakage current (I_{GS}).

Photocurrent response measurements

This type of measurement was conducted using two Keithley 2400 source meters: One was used to supply the power to the laser diode, and the other was used to supply the voltage to devices and monitor the channel current. The white light source was supplied by using a white LED array with a Dino-lite digital microscope and 532 or 405 nm excitation was supplied by KOKUYO laser diodes. The power density of the laser diode was adjusted by inserting a series of neutral density filters between the laser diode and the device. Laser power was measured with a FieldMate laser power meter from Coherent Inc. The pulse-mode laser signal was generated by using an Agilent 33220A function generator with controlled software to power the laser diode, and the energy of the pulse-mode laser was calibrated by using an Ophir Laserstar P/N 7021600 power meter with a lower limit of detection of 1 pW. All photocurrent measurements were performed inside a nitrogen atmosphere glove box with 3-mbar pressure. As shown in fig. S30, when operated in a glove box environment, these devices show a relatively small change in photocurrent over the course of months.

Microwave conductivity measurements

Microwave conductivity is a technique that can probe the photoexcited, mobile charge carriers in a semiconductor. The probe in this case is a microwave field that can resonantly interact with the mobile charge carriers. This interaction results in a slight attenuation of the microwave field. The magnitude of the microwave field attenuation is proportional to the number of mobile charges and their mobility. Fundamental considerations and a detailed discussion of this technique have been extensively described by Reid *et al.* (*61*).

Here, we deposit perovskite NCs as single layers or as heterojunctions with s-SWCNTs onto quartz substrates that are precisely cut to fill the cross-section of a microwave X-band waveguide (ca. 10.2 mm by 22.8 mm). For the measurement, an individual sample is placed inside the microwave cavity, which is directly attached to the waveguide. The microwave frequency of the probing field is then tuned to resonance with the sample cavity around 9 GHz. At resonance, the photoconductance ΔG of the sample is proportional to the changes in the microwave power and can be expressed as $\Delta G = -1/K \times \Delta P/P$, where K is an empirically determined calibration factor for the microwave cavity used in this experiment. The fraction of the microwave power $\Delta P/P$ quantifies the attenuation of the reflected microwave field.

The sample was then excited with by a laser pulse with a width of around 5 ns from an optical parametric oscillator (Spectra-Physics PremiScan ULD/500) pumped by the third harmonic of an Nd:YAG laser (Spectra-Physics Quanta-Ray). The pumping wavelength was 500 nm, with a fluence of about 2.5×10^{15} photons/cm^2. The changes in photoconductance were measured by continuously scanning the frequency range around the resonance of the microwave field, i.e., by adjusting the voltage of the microwave-generating oscillator (VCO, Sivers V03262X/00).

Temperature-dependent photocurrent measurement

All temperature-dependent photocurrent measurements were performed by using the Lake Shore 8400 helium cryogenic probe station, and the applied pulse-mode laser was supplied by using a laser diode controlled by an Agilent 33220A function generator with control software.

TOF-SIMS characterization

An ION-TOF TOF-SIMS V Time of Flight SIMS (TOF-SIMS) spectrometer was used for chemical imaging of the perovskite using methods covered in detail in previous reports (*55*). After a brief sputter cleaning with 1-KeV cesium ion beam (200 μm × 200 μm area, 8-nA current), high-resolution imaging was completed with a 30-KeV Bi_3^{++} primary ion beam (0.08-pA pulsed beam current) and a 25 μm × 25 μm area was analyzed with a 512:512 primary beam raster; after five image frames were collected, a brief sputtering with Cs was completed for one raster of the sputtering beam at 200 μm × 200 μm (~1.6 s of sputtering) to replenish the sample with cesium, which allows enhanced detection of halogen species. The total sputtering time for a sample during one measurement was 8.2 s.

Ultraviolet photoelectron spectroscopy measurements

Samples for photoelectron spectroscopy measurements were deposited onto clean gold substrates. X-ray photoelectron spectroscopy data were obtained on a Physical Electronics 5600 system using Al Kα radiation with an additional ultraviolet photoelectron spectroscopy (UPS) setup. The UPS was calibrated with cleaned Au metal and has energy uncertainty of ±0.025 eV.

SUPPLEMENTARY MATERIALS

Supplementary material for this article is available at http://advances.sciencemag.org/cgi/content/full/7/18/eabf1959/DC1

REFERENCES AND NOTES

1. F. Zhou, Z. Zhou, J. Chen, T. H. Choy, J. Wang, N. Zhang, Z. Lin, S. Yu, J. Kang, H.-S. P. Wong, Y. Chai, Optoelectronic resistive random access memory for neuromorphic vision sensors. *Nat. Nanotechnol.* **14**, 776–782 (2019).
2. Z. Cheng, C. Ríos, W. H. P. Pernice, C. D. Wright, H. Bhaskaran, On-chip photonic synapse. *Sci. Adv.* **3**, e1700160 (2017).
3. C. Ríos, M. Stegmaier, P. Hosseini, D. Wang, T. Scherer, C. D. Wright, H. Bhaskaran, W. H. P. Pernice, Integrated all-photonic non-volatile multi-level memory. *Nat. Photonics* **9**, 725–732 (2015).
4. T. Alexoudi, G. T. Kanellos, N. Pleros, Optical RAM and integrated optical memories: A survey. *Light Sci. Appl.* **9**, 91 (2020).
5. J. Feldmann, N. Youngblood, C. D. Wright, H. Bhaskaran, W. H. P. Pernice, All-optical spiking neurosynaptic networks with self-learning capabilities. *Nature* **569**, 208–214 (2019).
6. M. Lee, W. Lee, S. Choi, J.-W. Jo, J. Kim, S. K. Park, Y.-H. Kim, Brain-inspired photonic neuromorphic devices using photodynamic amorphous oxide semiconductors and their persistent photoconductivity. *Adv. Mater.* **29**, 1700951 (2017).
7. S. Lany, A. Zunger, Anion vacancies as a source of persistent photoconductivity in II-VI and chalcopyrite semiconductors. *Phys. Rev. B* **72**, 035215 (2005).
8. D. V. Lang, R. A. Logan, Large-lattice-relaxation model for persistent photoconductivity in compound semiconductors. *Phys. Rev. Lett.* **39**, 635–639 (1977).
9. J. Kakalios, H. Fritzsche, Persistent photoconductivity in doping-modulated amorphous semiconductors. *Phys. Rev. Lett.* **53**, 1602–1605 (1984).
10. Q. Wang, Y. Wen, K. Cai, R. Cheng, L. Yin, Y. Zhang, J. Li, Z. Wang, F. Wang, F. Wang, T. A. Shifa, C. Jiang, H. Yang, J. He, Nonvolatile infrared memory in Mos$_2$/Pbs van der waals heterostructures. *Sci. Adv.* **4**, eaap7916 (2018).
11. Y. Fu, H. Zhu, J. Chen, M. P. Hautzinger, X.-Y. Zhu, S. Jin, Metal halide perovskite nanostructures for optoelectronic applications and the study of physical properties. *Nat. Rev. Mater.* **4**, 169–188 (2019).
12. Y. Deng, Z. Xiao, J. Huang, Light-induced self-poling effect on organometal trihalide perovskite solar cells for increased device efficiency and stability. *Adv. Energy Mater.* **5**, 1500721 (2015).
13. Y. Yuan, J. Huang, Ion migration in organometal trihalide perovskite and its impact on photovoltaic efficiency and stability. *Acc. Chem. Res.* **49**, 286–293 (2016).
14. Y. Yuan, T. Li, Q. Wang, J. Xing, A. Gruverman, J. Huang, Anomalous photovoltaic effect in organic-inorganic hybrid perovskite solar cells. *Sci. Adv.* **3**, e1602164 (2017).
15. J.-W. Lee, S.-G. Kim, J.-M. Yang, Y. Yang, N.-G. Park, Verification and mitigation of ion migration in perovskite solar cells. *APL Mater.* **7**, 041111 (2019).
16. S. P. Dunfield, L. Bliss, F. Zhang, J. M. Luther, K. Zhu, M. F. A. M. van Hest, M. O. Reese, J. J. Berry, From defects to degradation: A mechanistic understanding of degradation in perovskite solar cell devices and modules. *Adv. Energy Mater.* **10**, 1904054 (2020).
17. P. Vashishtha, J. E. Halpert, Field-driven ion migration and color instability in red-emitting mixed halide perovskite nanocrystal light-emitting diodes. *Chem. Mater.* **29**, 5965–5973 (2017).
18. V. K. Sangwan, M. C. Hersam, Neuromorphic nanoelectronic materials. *Nat. Nanotechnol.* **15**, 517–528 (2020).
19. Z. Xiao, J. Huang, Energy-efficient hybrid perovskite memristors and synaptic devices. *Adv. Electron. Mater.* **2**, 1600100 (2016).
20. H. Tian, L. Zhao, X. Wang, Y.-W. Yeh, N. Yao, B. P. Rand, T.-L. Ren, Extremely low operating current resistive memory based on exfoliated 2D perovskite single crystals for neuromorphic computing. *ACS Nano* **11**, 12247–12256 (2017).
21. S.-I. Kim, Y. Lee, M.-H. Park, G.-T. Go, Y.-H. Kim, W. Xu, H.-D. Lee, H. Kim, D.-G. Seo, W. Lee, T.-W. Lee, Dimensionality dependent plasticity in halide perovskite artificial synapses for neuromorphic computing. *Adv. Electron. Mater.* **5**, 1900008 (2019).
22. J. Xing, Q. Wang, Q. Dong, Y. Yuan, Y. Fang, J. Huang, Ultrafast ion migration in hybrid perovskite polycrystalline thin films under light and suppression in single crystals. *Phys. Chem. Chem. Phys.* **18**, 30484–30490 (2016).
23. M. C. Brennan, S. Draguta, P. V. Kamat, M. Kuno, Light-induced anion phase segregation in mixed halide perovskites. *ACS Energy Lett.* **3**, 204–213 (2018).
24. Y.-C. Zhao, W.-K. Zhou, X. Zhou, K.-H. Liu, D.-P. Yu, Q. Zhao, Quantification of light-enhanced ionic transport in lead iodide perovskite thin films and its solar cell applications. *Light Sci. Appl.* **6**, e16243 (2017).
25. D. W. deQuilettes, W. Zhang, V. M. Burlakov, D. J. Graham, T. Leijtens, A. Osherov, V. Bulović, H. J. Snaith, D. S. Ginger, S. D. Stranks, Photo-induced halide redistribution in organic–inorganic perovskite films. *Nat. Commun.* **7**, 11683 (2016).
26. J. Borghetti, V. Derycke, S. Lenfant, P. Chenevier, A. Filoramo, M. Goffman, D. Vuillaume, J.-P. Bourgoin, Optoelectronic switch and memory devices based on polymer-functionalized carbon nanotube transistors. *Adv. Mater.* **18**, 2535–2540 (2006).
27. K. Wang, S. Dai, Y. Zhao, Y. Wang, C. Liu, J. Huang, Light-stimulated synaptic transistors fabricated by a facile solution process based on inorganic perovskite quantum dots and organic semiconductors. *Small* **15**, 1900010 (2019).
28. Z. Liu, S. Dai, Y. Wang, B. Yang, D. Hao, D. Liu, Y. Zhao, L. Fang, Q. Ou, S. Jin, J. Zhao, J. Huang, Photoresponsive transistors based on lead-free perovskite and carbon nanotubes. *Adv. Funct. Mater.* **30**, 1906335 (2020).
29. Y.-T. Li, L. Ding, J.-Z. Li, J. Kang, D.-H. Li, L. Ren, Z.-Y. Ju, M.-X. Sun, J.-Q. Ma, Y. Tian, G.-Y. Gou, D. Xie, H. Tian, Y. Yang, L.-W. Wang, L.-M. Peng, T.-L. Ren, Light-enhanced ion migration in two-dimensional perovskite single crystals revealed in carbon nanotubes/two-dimensional perovskite heterostructure and its photomemory application. *ACS Cent. Sci.* **5**, 1857–1865 (2019).
30. B. Pradhan, S. Das, J. Li, F. Chowdhury, J. Cherusseri, D. Pandey, D. Dev, A. Krishnaprasad, E. Barrios, A. Towers, A. Gesquiere, L. Tetard, T. Roy, J. Thomas, Ultrasensitive and ultrathin phototransistors and photonic synapses using perovskite quantum dots grown from graphene lattice. *Sci. Adv.* **6**, eaay5225 (2020).
31. L. Qian, Y. Sun, M. Wu, C. Li, D. Xie, L. Ding, G. Shi, A lead-free two-dimensional perovskite for a high-performance flexible photoconductor and a light-stimulated synaptic device. *Nanoscale* **10**, 6837–6843 (2018).
32. H. Zhang, X. Fu, Y. Tang, H. Wang, C. Zhang, W. W. Yu, X. Wang, Y. Zhang, M. Xiao, Phase segregation due to ion migration in all-inorganic mixed-halide perovskite nanocrystals. *Nat. Commun.* **10**, 1088 (2019).
33. S. Zhou, G. Zhou, Y. Li, X. Xu, Y.-J. Hsu, J. Xu, N. Zhao, X. Lu, Understanding charge transport in all-inorganic halide perovskite nanocrystal thin-film field effect transistors. *ACS Energy Lett.* **5**, 2614–2623 (2020).
34. M. Rother, M. Brohmann, S. Yang, S. B. Grimm, S. P. Schießl, A. Graf, J. Zaumseil, Aerosol-jet printing of polymer-sorted (6,5) carbon nanotubes for field-effect transistors with high reproducibility. *Adv. Electron. Mater.* **3**, 1700080 (2017).
35. G. J. Brady, A. J. Way, N. S. Safron, H. T. Evensen, P. Gopalan, M. S. Arnold, Quasi-ballistic carbon nanotube array transistors with current density exceeding Si and GaAs. *Sci. Adv.* **2**, e1601240 (2016).
36. A. D. Franklin, Nanomaterials in transistors: From high-performance to thin-film applications. *Science* **349**, aab2750 (2015).
37. S. P. Schießl, N. Fröhlich, M. Held, F. Gannott, M. Schweiger, M. Forster, U. Scherf, J. Zaumseil, Polymer-sorted semiconducting carbon nanotube networks for high-performance ambipolar field-effect transistors. *ACS Appl. Mater. Interfaces* **7**, 682–689 (2015).
38. R. Ihly, A.-M. Dowgiallo, M. Yang, P. Schulz, N. J. Stanton, O. G. Reid, A. J. Ferguson, K. Zhu, J. J. Berry, J. L. Blackburn, Efficient charge extraction and slow recombination in organic-inorganic perovskites capped with semiconducting single-walled carbon nanotubes. *Energ. Environ. Sci.* **9**, 1439–1449 (2016).
39. P. Schulz, A.-M. Dowgiallo, M. Yang, K. Zhu, J. L. Blackburn, J. J. Berry, Charge transfer dynamics between carbon nanotubes and hybrid organic metal halide perovskite films. *J. Phys. Chem. Lett.* **7**, 418–425 (2016).
40. S. N. Habisreutinger, N. K. Noel, B. W. Larson, O. G. Reid, J. L. Blackburn, Rapid charge-transfer cascade through swcnt composites enabling low-voltage losses for perovskite solar cells. *ACS Energy Lett.* **4**, 1872–1879 (2019).
41. S. Dai, X. Wu, D. Liu, Y. Chu, K. Wang, B. Yang, J. Huang, Light-stimulated synaptic devices utilizing interfacial effect of organic field-effect transistors. *ACS Appl. Mater. Interfaces* **10**, 21472–21480 (2018).
42. S. Qin, F. Wang, Y. Liu, Q. Wan, X. Wang, Y. Xu, Y. Shi, X. Wang, R. Zhang, A light-stimulated synaptic device based on graphene hybrid phototransistor. *2D Mater.* **4**, 035022 (2017).
43. H. K. Li, T. P. Chen, P. Liu, S. G. Hu, Y. Liu, Q. Zhang, P. S. Lee, A light-stimulated synaptic transistor with synaptic plasticity and memory functions based on InGaZno$_x$–Al$_2$o$_3$ thin film structure. *J. Appl. Phys.* **119**, 244505 (2016).
44. Y. Wang, Z. Lv, J. Chen, Z. Wang, Y. Zhou, L. Zhou, X. Chen, S.-T. Han, Photonic synapses based on inorganic perovskite quantum dots for neuromorphic computing. *Adv. Mater.* **30**, 1802883 (2018).
45. A.-M. Dowgiallo, K. S. Mistry, J. C. Johnson, J. L. Blackburn, Ultrafast spectroscopic signature of charge transfer between single-walled carbon nanotubes and C$_{60}$. *ACS Nano* **8**, 8573–8581 (2014).
46. D. B. Sulas-Kern, H. Zhang, Z. Li, J. L. Blackburn, Microsecond charge separation at heterojunctions between transition metal dichalcogenide monolayers and single-walled carbon nanotubes. *Mater. Horiz.* **6**, 2103–2111 (2019).

47. A. J. Ferguson, O. G. Reid, S. U. Nanayakkara, R. Ihly, J. L. Blackburn, Efficiency of charge-transfer doping in organic semiconductors probed with quantitative microwave and direct-current conductance. *J. Phys. Chem. Lett.* **9**, 6864–6870 (2018).
48. E. A. Gaulding, J. Hao, H. S. Kang, E. M. Miller, S. N. Habisreutinger, Q. Zhao, A. Hazarika, P. C. Sercel, J. M. Luther, J. L. Blackburn, Conductivity tuning via doping with electron donating and withdrawing molecules in perovskite Cspbi$_3$ nanocrystal films. *Adv. Mater.* **31**, 1902250 (2019).
49. K. Roy, M. Padmanabhan, S. Goswami, T. P. Sai, G. Ramalingam, S. Raghavan, A. Ghosh, Graphene–Mos$_2$ hybrid structures for multifunctional photoresponsive memory devices. *Nat. Nanotechnol.* **8**, 826–830 (2013).
50. K. P. Bera, G. Haider, Y.-T. Huang, P. K. Roy, C. R. Paul Inbaraj, Y.-M. Liao, H.-I. Lin, C.-H. Lu, C. Shen, W. Y. Shih, W.-H. Shih, Y.-F. Chen, Graphene sandwich stable perovskite quantum-dot light-emissive ultrasensitive and ultrafast broadband vertical phototransistors. *ACS Nano* **13**, 12540–12552 (2019).
51. G. Konstantatos, M. Badioli, L. Gaudreau, J. Osmond, M. Bernechea, F. P. G. de Arquer, F. Gatti, F. H. L. Koppens, Hybrid graphene–quantum dot phototransistors with ultrahigh gain. *Nat. Nanotechnol.* **7**, 363–368 (2012).
52. K. Domanski, J.-P. Correa-Baena, N. Mine, M. K. Nazeeruddin, A. Abate, M. Saliba, W. Tress, A. Hagfeldt, M. Grätzel, Not all that glitters is gold: Metal-migration-induced degradation in perovskite solar cells. *ACS Nano* **10**, 6306–6314 (2016).
53. R. A. Kerner, P. Schulz, J. A. Christians, S. P. Dunfield, B. Dou, L. Zhao, G. Teeter, J. J. Berry, B. P. Rand, Reactions at noble metal contacts with methylammonium lead triiodide perovskites: Role of underpotential deposition and electrochemistry. *APL Mater.* **7**, 041103 (2019).
54. Z. Li, C. Xiao, Y. Yang, S. P. Harvey, D. H. Kim, J. A. Christians, M. Yang, P. Schulz, S. U. Nanayakkara, C.-S. Jiang, J. M. Luther, J. J. Berry, M. C. Beard, M. M. Al-Jassim, K. Zhu, Extrinsic ion migration in perovskite solar cells. *Energ. Environ. Sci.* **10**, 1234–1242 (2017).
55. S. P. Harvey, Z. Li, J. A. Christians, K. Zhu, J. M. Luther, J. J. Berry, Probing perovskite inhomogeneity beyond the surface: TOF-SIMS analysis of halide perovskite photovoltaic devices. *ACS Appl. Mater. Interfaces* **10**, 28541–28552 (2018).
56. D. M. Kroupa, M. Vörös, N. P. Brawand, B. W. McNichols, E. M. Miller, J. Gu, A. J. Nozik, A. Sellinger, G. Galli, M. C. Beard, Tuning colloidal quantum dot band edge positions through solution-phase surface chemistry modification. *Nat. Commun.* **8**, 15257 (2017).
57. Y. Zhao, J. Wei, R. Vajtai, P. M. Ajayan, E. V. Barrera, Iodine doped carbon nanotube cables exceeding specific electrical conductivity of metals. *Sci. Rep.* **1**, 83 (2011).
58. J. Zhang, S. Dai, Y. Zhao, J. Zhang, J. Huang, Recent progress in photonic synapses for neuromorphic systems. *Adv. Intell. Syst.* **2**, 1900136 (2020).
59. G. Stefanovich, A. Pergament, D. Stefanovich, Electrical switching and mott transition in Vo$_2$. *J. Phys. Condens. Matter* **12**, 8837–8845 (2000).
60. Z. Yang, C. Ko, S. Ramanathan, Oxide electronics utilizing ultrafast metal-insulator transitions. *Annu. Rev. Mater. Res.* **41**, 337–367 (2011).
61. O. G. Reid, D. T. Moore, Z. Li, D. Zhao, Y. Yan, K. Zhu, G. Rumbles, Quantitative analysis of time-resolved microwave conductivity data. *J. Phys. D Appl. Phys.* **50**, 493002 (2017).
62. J. Wang, S. R. Peurifoy, M. T. Bender, F. Ng, K.-S. Choi, C. Nuckolls, M. S. Arnold, Non-fullerene acceptors for harvesting excitons from semiconducting carbon nanotubes. *J. Phys. Chem. C* **123**, 21395–21402 (2019).
63. L. Du, X. Luo, F. Zhao, W. Lv, J. Zhang, Y. Peng, Y. Tang, Y. Wang, Toward facile broadband high photoresponse of fullerene based phototransistor from the ultraviolet to the near-infrared region. *Carbon* **96**, 685–694 (2016).
64. Y. Guo, C. Liu, H. Tanaka, E. Nakamura, Air-stable and solution-processable perovskite photodetectors for solar-blind UV and visible light. *J. Phys. Chem. Lett.* **6**, 535–539 (2015).
65. X. Luo, F. Zhao, L. Du, W. Lv, K. Xu, Y. Peng, Y. Wang, F. Lu, Ultrasensitive flexible broadband photodetectors achieving pA scale dark current. *npj Flexible Electron.* **1**, 6 (2017).
66. H. Fang, W. Hu, Photogating in low dimensional photodetectors. *Adv. Sci.* **4**, 1700323 (2017).
67. H. Kind, H. Yan, B. Messer, M. Law, P. Yang, Nanowire ultraviolet photodetectors and optical switches *Adv. Mater.* **14**, 158–160 (2002).
68. Z. Xu, Y. Yu, S. Arya, I. A. Niaz, Y. Chen, Y. Lei, M. A. R. Miah, J. Zhou, A. C. Zhang, L. Yan, S. Xu, K. Nomura, Y.-H. Lo, Frequency- and power-dependent photoresponse of a perovskite photodetector down to the single-photon level. *Nano Lett.* **20**, 2144–2151 (2020).
69. F. Li, H. Wang, D. Kufer, L. Liang, W. Yu, E. Alarousu, C. Ma, Y. Li, Z. Liu, C. Liu, N. Wei, F. Wang, L. Chen, O. F. Mohammed, A. Fratalocchi, X. Liu, G. Konstantatos, T. Wu, Ultrahigh carrier mobility achieved in photoresponsive hybrid perovskite films via coupling with single-walled carbon nanotubes. *Adv. Mater.* **29**, 1602432 (2017).
70. H. Zhu, A. Liu, H. L. Luque, H. Sun, D. Ji, Y.-Y. Noh, Perovskite and conjugated polymer wrapped semiconducting carbon nanotube hybrid films for high-performance transistors and phototransistors. *ACS Nano* **13**, 3971–3981 (2019).
71. C. Ma, S. Clark, Z. Liu, L. Liang, Y. Firdaus, R. Tao, A. Han, X. Liu, L.-J. Li, T. D. Anthopoulos, M. C. Hersam, T. Wu, Solution-processed mixed-dimensional hybrid perovskite/carbon nanotube electronics. *ACS Nano* **14**, 3969–3979 (2020).
72. M. Spina, B. Náfrádi, H. M. Tóháti, K. Kamarás, E. Bonvin, R. Gaal, L. Forró, E. Horváth, Ultrasensitive 1d field-effect phototransistors: CH$_3$NH$_3$PbI$_3$ nanowire sensitized individual carbon nanotubes. *Nanoscale* **8**, 4888–4893 (2016).
73. A. Joushaghani, J. Jeong, S. Paradis, D. Alain, J. S. Aitchison, J. K. S. Poon, Characteristics of the current-controlled phase transition of VO$_2$ microwires for hybrid optoelectronic devices. *Photonics* **2**, 916–932 (2015).

Acknowledgments

Funding: This work was supported by the Center for Hybrid Organic Inorganic Semiconductors for Energy (CHOISE), an Energy Frontier Research Center funded by the Office of Science, Office of Basic Energy Sciences within the U.S. Department of Energy (DOE). This work was authored, in part, by Alliance for Sustainable Energy LLC, the manager and operator of the National Renewable Energy Laboratory for the U.S. DOE under contract no. DE-AC36-08GO28308. S.N.H. acknowledges support from the Director's Fellowship program of the National Renewable Energy Laboratory. (6,5) s-SWCNT alignment and short-channel FET fabrication supported by National Science Foundation (NSF) Scalable Nanomanufacturing (SNM) award No. 1727523 (S.M.F, M.S.A.). We also acknowledge E. A. Gaulding for help with initial NC synthesis, S. Bauers for help with initial temperature-dependent measurements, Z. Li for help with SEM measurements, and S. Banerjee (Texas A&M) for helpful discussions. The views expressed in the article do not necessarily represent the views of the DOE or the U.S. government. The U.S. government retains and the publisher, by accepting the article for publication, acknowledges that the U.S. government retains a nonexclusive, paid-up, irrevocable, worldwide license to publish or reproduce the published form of this work, or allow others to do so, for U.S. government purposes. **Author contributions:** J.H. was involved in all experimental work. Y.-H.K. prepared perovskite NCs and was involved in fabricating devices. S.N.H. conducted microwave conductivity measurements and time-resolved PL measurements. S.P.H. conducted TOF-SIMS measurements. S.M.F. and M.S.A. fabricated short-channel SWCNT FETs. Y.Y. and Z.S. contributed to mechanistic understanding. E.M.M. performed photoelectron spectroscopy measurements J.L.B. and J.H. prepared the manuscript. J.M.L. and J.L.B. managed the project. All authors were involved with manuscript revision and experimental discussion. **Competing interests:** J.L.B., J.M.L., J.H., and Y.-H.K. are inventors on a patent application related to this work filed by the National Renewable Energy Laboratory. The authors declare that they have no other competing interests. **Data and materials availability:** All data needed to evaluate the conclusions in the paper are present in the paper and/or the Supplementary Materials. Additional data related to this paper may be requested from the authors.

Submitted 9 October 2020
Accepted 10 March 2021
Published 28 April 2021
10.1126/sciadv.abf1959

Citation: J. Hao, Y.-H. Kim, S. N. Habisreutinger, S. P. Harvey, E. M. Miller, S. M. Foradori, M. S. Arnold, Z. Song, Y. Yan, J. M. Luther, J. L. Blackburn, Low-energy room-temperature optical switching in mixed-dimensionality nanoscale perovskite heterojunctions. *Sci. Adv.* **7**, eabf1959 (2021).